A&A 516, A68 (2010)
DOI: 10.1051/0004-6361/201014094

Astronomy & Astrophysics

Circumstellar molecular composition of the oxygen-rich AGB star IK Tauri

I. Observations and LTE chemical abundance analysis

H. Kim[1,2], F. Wyrowski[1], K. M. Menten[1], and L. Decin[3,4]

[1] Max-Planck-Institut für Radioastronomie, Auf dem Hügel 69, 53121 Bonn, Germany
e-mail: hyunjoo.kim@aei.mpg.de
[2] Max-Planck-Institut für Gravitationsphysik, Callinstr. 38, 30167 Hannover, Germany
[3] Instituut voor Sterrenkunde, KU Leuven, Celestijnenlaan 200D, 3001 Leuven, Belgium
[4] Sterrenkundig Instituut Anton Pannekoek, University of Amsterdam, PO Box 9429, 1090 CE Amsterdam, The Netherlands

Received 18 January 2010 / Accepted 8 April 2010

ABSTRACT

Context. Molecular lines in the (sub)millimeter wavelength range can provide important information about the physical and chemical conditions in the circumstellar envelopes around asymptotic giant branch stars.
Aims. The aim of this paper is to study the molecular composition in the circumstellar envelope around the oxygen-rich star IK Tau.
Methods. We observed IK Tau in several (sub)millimeter bands using the APEX telescope during three observing periods. To determine the spatial distribution of the ^{12}CO(3−2) emission, mapping observations were performed. To constrain the physical conditions in the circumstellar envelope, multiple rotational CO emission lines were modeled using a nonlocal thermodynamic equilibrium radiative transfer code. The rotational temperatures and the abundances of the other molecules were obtained assuming local thermodynamic equilibrium.
Results. An oxygen-rich asymptotic giant branch star has been surveyed in the submillimeter wavelength range. Thirty four transitions of twelve molecular species, including maser lines, were detected. The kinetic temperature of the envelope was determined, and the molecular abundance fractions of the molecules were estimated. The deduced molecular abundances were compared with observations and modeling from the literature and agree within a factor of 10, except for SO_2, which is found to be almost a factor 100 stronger than predicted by chemical models.
Conclusions. From this study, we found that IK Tau is a good laboratory for studying the conditions in circumstellar envelopes around oxygen-rich stars with (sub)millimeter-wavelength molecular lines. We could also expect from this study that the molecules in the circumstellar envelope can be explained more faithfully by non-LTE analysis with lower and higher transition lines than by simple LTE analysis with only lower transition lines. In particular, the observed CO line profiles could be well reproduced by a simple expanding envelope model with a power-law structure.

Key words. line: profiles – methods: observational – telescopes – stars: mass-loss – stars: abundances – submillimeter: stars

1. Introduction

Stars with initial masses lower than ∼8 $M_\odot$ evolve to a pulsationally unstable red giant star on the asymptotic giant branch (AGB). At this stage, mass loss from the evolved central star produces an expanding envelope. Further on, carbon, C, is fused in the core and then oxygen, O (Yamamura et al. 1996; Fukasaku et al. 1994).

AGB stars are characterized by low surface temperatures, $T_* \leq 3000$ K, high luminosities up to several 10^4 $L_\odot$, and a very large geometric size up to several AU (Habing 1996). In general, these highly evolved stars are surrounded by envelopes with expansion velocities between 5 km s^{-1} and 40 km s^{-1}. They have high mass-loss rates between 10^{-8} and 10^{-4} $M_\odot$ yr^{-1}. Their atmospheres provide favorable thermodynamic conditions for the formation of simple molecules, owing to the low temperatures and, simultaneously, high densities. Because of pulsation, molecules may reach a distance at which the temperature is lower than the condensation temperature and at which the density is still high enough for dust grains to form. Radiation pressure drives the dust away from the star. Molecules surviving dust formation are accelerated by dust-grain collisions (Goldreich & Scoville 1976).

The chemistry of the atmospheres and, farther out, of the circumstellar envelopes (CSEs) around AGB stars is dependent on the chemical class. They are classified either as M stars (C/O abundance ratio <1), S stars (C/O ≈ 1), or C stars (C/O >1). The optical and infrared spectra of AGB stars show absorption from the stellar atmosphere. M-type stellar spectra are dominated by lines of oxygen-bearing molecules, e.g., the metal oxides SiO and TiO, and by H_2O. In C-star atmospheres, carbon-bearing molecules like, a.o., CH, C_2, C_2H_2, and HCN are detected at optical and infrared wavelengths, and in the microwave regime (e.g. Gautschy-Loidl et al. 2004). While the *atmospheric* abundance fractions are nowadays quite well understood in terms of initial chemical composition, which may be altered by nucleosynthetic products that are brought to the surface by dredge-ups, the main processes determining the *circumstellar* chemical abundance stratification of many molecules are still largely not understood. In the stellar photosphere, the high gas density ensures thermal equilibrium (TE). Pulsation-driven shocks in the inner wind region suppress TE. This region of strong shock activity is also the locus of grain formation, resulting in the depletion of few molecules such as SiO and SiS. Other molecules, such as CO and CS, are thought to be unreactive in the dust-forming region (Duari et al. 1999). At larger radii, the so-called

outer envelope is penetrated by ultraviolet interstellar photons and cosmic rays resulting in a chemistry governed by photochemical and ion-molecule reactions. This picture of the chemical processes altering the abundance stratification is generally accepted, but many details on chemical reactions rates, molecular left-overs after the dust formation, shock strengths inducing a fast chemistry zone, etc., are not yet known.

Spectroscopical studies of molecular lines in the (sub)millimeter range are very useful tools for estimating the physical and chemical conditions in CSEs. Due to its proximity, the carbon-rich AGB star IRC+10216 has attracted a lot of attention, resulting in the detection of more than 60 different chemical compounds in its CSE (e.g. Ridgway et al. 1976; Cernicharo et al. 2000). Until now, detailed studies of oxygen-rich envelopes have been rare. Recently, Ziurys et al. (2004) have focused on the chemical analysis of the oxygen-rich peculiar red supergiant VY CMa. VY CMa is, however, not a prototype of an evolved oxygen-rich star. A complex geometry is deduced from Hubble Space Telescope images (Smith et al. 2001) with a luminosity higher than 10^5 $L_\odot$ and a mass-loss rate of $\sim 2 \times 10^{-4}$ $M_\odot$/yr (Bowers et al. 1983; Sopka et al. 1985). VY CMa is a spectacular object, which can explode as a supernova at any time because of its extreme evolutionary state. Interpreting the molecular emission profiles of VY CMa is therefore a very complex task, subject to many uncertainties. To enlarge our insight into the chemical structure in the envelopes of oxygen-rich low and intermediate-mass stars, we therefore have started a submillimeter survey of the oxygen-rich AGB star IK Tau, which is thought to be (roughly) spherically symmetric (Lane et al. 1987; Marvel 2005). We thereby hope to advance understanding of the final stages of stellar evolution of the majority of stars in galaxies like our Milky Way and their resulting impact on the interstellar medium and the cosmic cycle.

Mira variable IK Tau, also known as NML Tau, is located at $\alpha_{2000} = 3^{\rm h}53^{\rm m}28\overset{\rm s}{.}8$, $\delta_{2000} = 11°24'23''$. It was found to be an extremely cool star with large infrared $(J - K)$ excess (Alcolea et al. 1999) consistent with a 2000 K blackbody. IK Tau shows regular optical variations with an amplitude of ~4.5 mag. It is an O-rich star of spectral type ranging from M8.1 to M11.2 (Wing & Lockwood 1973). Its distance was derived by Olofsson et al. (1998) to be 250 pc assuming a stellar temperature of 2000 K. The pulsation period is ~470 days (Hale et al. 1997). The systemic velocity of the star is 33.7 km s^{-1}. Mass-loss rate estimates range from 2.4×10^{-6} $M_\odot\,{\rm yr}^{-1}$ (from the CO(J = 1–0) line; Olofsson et al. 1998) to 3×10^{-5} $M_\odot\,{\rm yr}^{-1}$ (from an analysis of multiple SiO lines; González Delgado et al. 2003).

In the circumstellar envelope of IK Tau maser emission from OH (Bowers et al. 1989), H_2O (Lane et al. 1987), and SiO (Boboltz & Diamond 2005), and thermal emission of SiO, CO, SiS, SO, SO_2, and HCN have previously been found (Lindqvist et al. 1988; Bujarrabal et al. 1994; Omont et al. 1993). Obviously, IK Tau is a prime candidate for circumstellar chemistry studies.

2. Observations

The observations were performed with the APEX[1] 12 m telescope in Chile (Güsten et al. 2006) located at the 5100 m high site on Llano de Chajnantor. The data were obtained during observing periods in 2005 November and 2006 April and August. The receivers used were the facility APEX-2A (Risacher et al. 2006) and the MPIfR FLASH receivers (Heyminck et al. 2006). Typical system noise temperatures were about 200 K–1000 K at 290 GHz and 350 GHz, and 1000 K at 460 GHz, and 5000 K at 810 GHz. The spectrometers for the observations were fast fourier transform spectrometers (FFTS) with 1 GHz bandwidth, and the channel width for the 290–350 GHz observations was approximately 122.07 kHz (8192 channels), and for the 460 GHz and 810 GHz observations 488.28 kHz (2048 channels). For the observations, a position-switching mode was used with the reference position typically 180″ off-source. The antenna was focused on the available planets. IK Tau itself was strong enough to serve as a line pointing source, so small cross scans in the ^{12}CO(3–2) line monitored the pointing during the observations. The telescope beam sizes (HPBW) at frequencies of the observed molecular lines are shown in Table 1. The antenna beam efficiencies are given in Table 2 of Güsten et al. (2006).

Table 1. Overview of the molecular line transitions observed with APEX.

Species	Transition	ν (MHz)	HPBW (″)
^{12}CO	3–2	345 796.00	18
	4–3	461 040.78	14
	7–6	806 651.81	8
^{13}CO	3_3–2_2	330 587.94	19
SiS	16–15	290 380.31	21
	17–16	308 515.63	20
	19–18	344 778.78	18
	20–19	362 906.34	18
^{28}SiO	7–6	303 926.81	20
	8–7	347 330.59	18
^{29}SiO	7–6	300 120.47	20
	8–7	342 980.84	18
^{30}SiO	7–6	296 575.75	21
	8–7	338 930.03	18
SO	7_7–6_6	301 286.13	20
	8_8–7_7	344 310.63	18
SO_2	$3_{3\,1}$–$2_{2\,0}$	313 279.72	20
	$17_{1\,17}$–$16_{0\,16}$	313 660.84	20
	$4_{3\,1}$–$3_{2\,2}$	332 505.25	19
	$13_{2\,12}$–$12_{1\,11}$	345 338.53	18
	$5_{3\,3}$–$4_{2\,2}$	351 257.22	18
	$14_{4\,10}$–$14_{3\,11}$	351 873.88	18
CS	6–5	293 912.25	21
	7–6	342 883.00	18
HCN	4–3	354 505.47	18
CN	N = 3–2, J = 5/2–3/2	340 031.56	18
	N = 3–2, J = 7/2–5/2	340 247.78	18
	masers		
H_2O	$10_{2\,9}$–$9_{3\,6}$	321 225.63	19
	$5_{1\,5}$–$4_{2\,2}$	325 152.91	19
^{28}SiO	v = 1, 7–6	301 814.30	20
	v = 1, 8–7	344 916.35	18
	v = 3, 7–6	297 595.41	20
^{29}SiO	v = 1, 7–6	298 047.33	20
^{30}SiO	v = 1, 8–7	336 602.44	19

Notes. The third column lists the transition frequency, the last column the beam size (HPBW). For CN, only the strongest hyperfine component is given.

[1] This publication is based on data acquired with the Atacama Pathfinder Experiment (APEX). APEX is a collaboration between the Max-Planck-Institut für Radioastronomie, the European Southern Observatory, and the Onsala Space Observatory.

Table 2. Beam efficiencies for the different receivers.

Receiver	Forward efficiency	Beam efficiency
APEX-2A 290 GHz	0.97	0.80
APEX-2A 350 GHz	0.97	0.73
FLASH 460 GHz	0.95	0.60
FLASH 810 GHz	0.95	0.43

To map the circumstellar envelope in the ^{12}CO(3–2) line, 30 positions distributed on a 5×6 grid in right ascension and declination were observed. The grid spacing was 9″ (half the FWHM beam size at 345 GHz). A raster mapping procedure was used along the parallel grid lines with an integration time of 15 s.

The spectra were reduced using the CLASS program of the IRAM GILDAS[2]. To calculate the main-beam brightness temperatures of the lines, $T_{\rm MB}$, the following relation was used:

$$T_{\rm MB} = T_{\rm A}^{*} \frac{\eta_{\rm f}}{\eta_{\rm eff}} \cdot \quad (1)$$

Here $T_{\rm A}^{*}$ is the measured antenna temperature, $\eta_{\rm f}$ the forward efficiency, and $\eta_{\rm eff}$ the antenna main-beam efficiency of APEX (see Table 2).

3. Observational results

Thirty-four transitions from 12 molecular species including maser lines were detected with the APEX telescope toward IK Tau. The detected molecular lines are listed in Table 1 and their spectra are displayed in Figs. 1 to 5.

Figures 6 and 7 show the H_2O maser lines and SiO maser lines observed toward IK Tau, respectively; the maser line parameters are given in Table 3. Maser emission from H_2O at 321 GHz and 325 GHz was detected, as it was in the J = 7–6 and J = 8–7 rotational transitions within the v = 1 and v = 3 vibrationally excited states of ^{28}SiO, ^{29}SiO, and ^{30}SiO.

3.1. Line parameters

To get the mean brightness temperature estimates, the spectra were corrected by the beam-filling factors assuming a CO source size of 17″ (Bujarrabal & Alcolea 1991), an HCN source size of 3.85″ (Marvel 2005) and source sizes for the other molecules of 2.2″ (Lucas et al. 1992). The CO size may be uncertain, probably underestimated, since the signal-to-noise (S/N) ratios of the profiles obtained by Bujarrabal & Alcolea (1991) are much lower than those of the CO profiles presented in this paper.

The beam-filling factor is given by

$$f = \frac{\theta_{\rm S}^2}{\theta_{\rm S}^2 + \theta_{\rm b}^2}, \quad (2)$$

where $\theta_{\rm S}$ is the source size and $\theta_{\rm b}$ the half-power beam width (HPBW) shown in Table 1. Both source and beam are assumed to be circular Gaussians. The mean brightness temperature estimate is computed by

$$T_{\rm b} = \frac{1}{f} T_{\rm MB}. \quad (3)$$

[2] GILDAS is a collection of software oriented toward (sub-) millimeter radio astronomical applications developed by IRAM (see more details on http://www.iram.fr/IRAMFR/GILDAS).

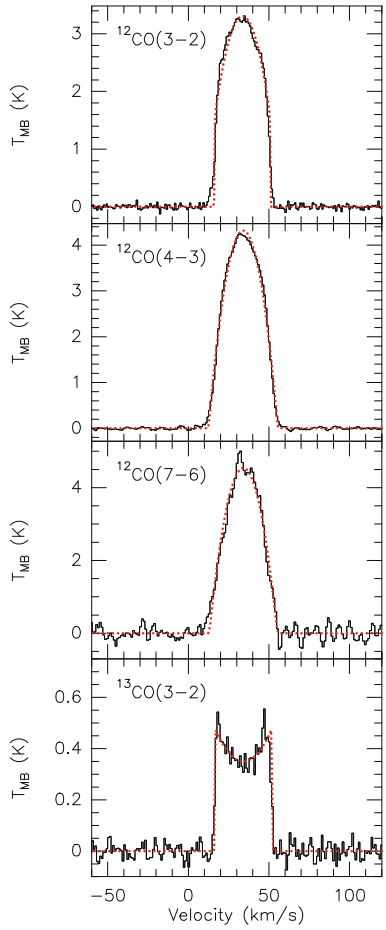

Fig. 1. Observed ^{12}CO and ^{13}CO line profiles (solid lines) and the expanding shell fit (dotted lines).

Line parameters were derived with CLASS (see more details on http://www.iram.fr/IRAMFR/GILDAS) from fitting the spectral lines with expanding shell fits, from which the expansion velocity of the envelope is obtained. The observed maser line and thermal emission line parameters are given in Tables 3 and 4, including the envelope expansion velocity $V_{\rm exp}$, the main beam brightness temperature $T_{\rm MB}$, the integrated area, and the parameters of the expanding shell fits. The expansion velocities are distributed from 14 km s^{-1} to 21 km s^{-1}.

When the S/N is high enough to warrant a consideration of the shape of the line profiles, they appear to be characteristic of circumstellar envelopes (for more detail see Zuckerman 1987): the ^{12}CO lines have the parabolic shape of optically thick lines, and the ^{13}CO(3–2) line has the double-horn shape of spatially resolved optically thin lines (see Fig. 1). Lines from the three SiO isotopologues and SiS lines have a Gaussian shape (see Fig. 4), indicating that they are partially formed in the wind acceleration regime where the stellar winds has not yet reached its full terminal velocity (Bujarrabal & Alcolea 1991). Some of the SO_2 lines seem to show the square shape characteristic of unresolved optically thin lines and some of them have the parabolic shape of optically thick lines (see Fig. 5). The CS and SO lines seem to have the square shape of unresolved optically thin lines for low excitation transitions and the parabolic shape of optically thick lines for high excitation transitions (see Fig. 3). HCN shows a global parabolic shape with a weak double-peak profile on the top (see Fig. 2). For the CN molecule, fits to the spectra were done that take the hyperfine structure of the molecule into

Table 3. Line parameters for the detected maser lines.

Species	Transition	T_{MB} peak (K) Bright temp. estimate	Profile T_{MB} area (K km s^{-1}) Bright temp. estimate	V_{lsr} (km s^{-1})
H_2O	10_{29}–9_{36}	1.36	4.31	33.4
	5_{15}–4_{22}	2.09	37.9	35.0
^{28}SiO	$V = 1$, 7–6	0.44	3.64	32.5
	$V = 1$, 8–7	0.29	1.00	34.6
	$V = 3$, 7–6	0.36	1.22	33.4
^{29}SiO	$V = 1$, 7–6	0.41	1.63	32.9
^{30}SiO	$V = 1$, 8–7	1.40	5.4	33.8

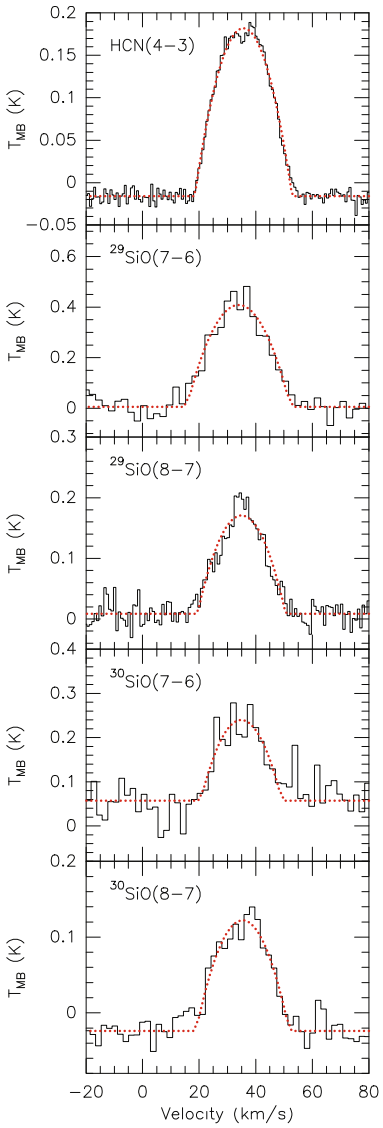

Fig. 2. Observed HCN, ^{29}SiO and ^{30}SiO, line profiles (solid lines) and the expanding shell fit (dotted lines).

account. Although the S/N of the individual components is low, the observations do not agree with the optical thin ratio of different HFS components and hint at hyperfine anomalies, as already reported by Bachiller et al. (1997).

3.2. CO maps

The spectra resulting from mapping the ^{12}CO(3−2) transition in a region of 45″×54″ around IK Tau are shown in Fig. 8. These spectra provide us with a tool for deriving the source size as a function of radial velocity (see Fig. 9). The envelope of IK Tau roughly appears spherically symmetric in ^{12}CO(3−2) with a deconvolved extent at a half-peak integrated intensity of 20″. The physical diameter of the emission region is thus 2.1×10^{16} cm where assuming a source distance of 250 pc.

4. Modeling results

4.1. Physical structure of the envelope

The CO lines are among the best tools for estimating the global properties of circumstellar envelopes, since the abundance of CO is quite constant across the envelope, except for photodissociation effects at the outer edge (Mamon et al. 1988). The spatial distribution of CO was found from our mapping observation to be spherically symmetric (see Sect. 3.2). A detailed multiline non-LTE (non-local thermodynamic equilibrium) study of CO can therefore be used to determine the physical properties of the envelope.

The one-dimensional version of the Monte Carlo code RATRAN (Hogerheijde & van der Tak 2000) was used to simulate the CO lines' emission. The basic idea of the Monte Carlo method is to split the emergent radiative energies into *photon packages*, which perform a random walk through the model volume. This allows the separation of local and external contributions of the radiation field and makes it possible to calculate the radiative transfer and excitation of molecular lines. The Monte Carlo method for molecular line transfer has been described by Bernes (1979) for a spherically symmetric cloud with a uniform density. The code is formulated from the viewpoint of cells rather than photons. It shows accurate and fast performance even for high opacities (for more details see Hogerheijde & van der Tak 2000). The circumstellar envelope is assumed to be spherically symmetric, to be produced by a constant mass-loss rate, and to expand at a constant velocity. In the Monte Carlo simulation, typically 10^3 model photons are followed throughout the envelope until they escape. The region is divided into discrete grid shells, each with constant properties (density, temperature, molecular abundance, turbulent line width, etc.).

For the case of a steady-state, spherically symmetric outflow, the gas density as a function of radial distance from the center of the AGB star is given by

$$n(r) = \frac{\dot{M}}{4\pi r^2 V_{\rm exp} m}, \quad (4)$$

where $\dot{M}$ is the mass-loss rate, m is the mass of the typical gas particle, taken to be $m \sim 3 \times 10^{-24}$ gram, since the gas is mainly in molecular form in AGB envelopes (Teyssier et al. 2006).

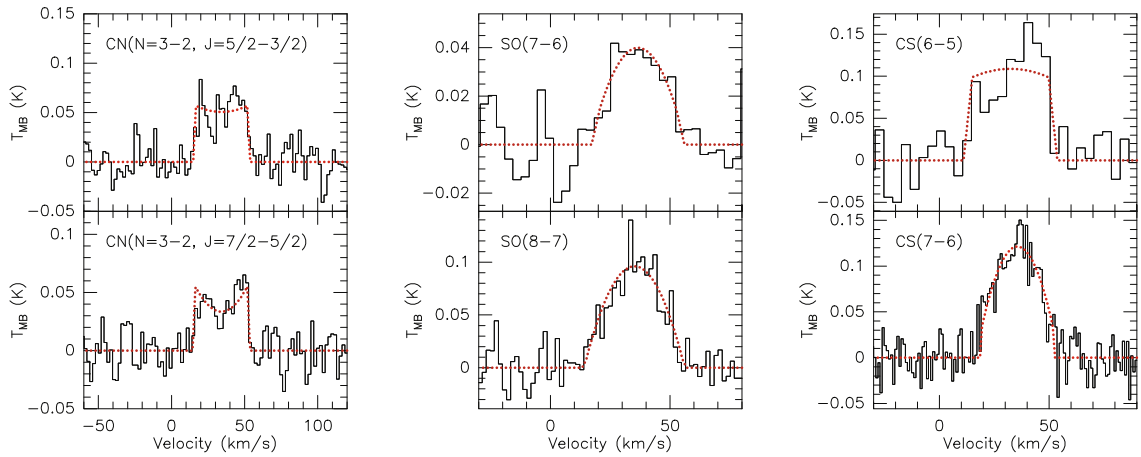

Fig. 3. Observed CN, SO, and CS line profiles (solid lines) and the expanding shell fit (dotted lines).

Table 4. Line parameters for each (nonmasering) transition.

Species	Transition	$\frac{Eu}{k}$ (K)	μ_0^2S (Debye^2)	T_{MB} peak (K) / Mean T_b	Profile T_{MB} area (K km s^{-1}) / Integrated mean T_b	V_{exp} (km s^{-1})
^{12}CO	3–2	33.2	0.04	3.31/5.99	95.7/173	17.3
	4–3	55.3	0.05	4.25/6.33	125/186	21.2
	7–6	155	0.08	5.04/5.85	129/149	21.0
^{13}CO	3–2	31.7	0.04	0.58/1.10	15.2/23.0	17.8
SiS	16–15	118	47.9	0.21/19.3	3.91/360	12.9
	17–16	133	50.9	0.28/23.4	5.77/483	16.4
	19–18	166	56.9	0.29/19.7	6.33/430	17.3
	20–19	183	59.9	0.27/18.3	5.2/353	19.4
SiO	7–6	58.4	67.4	0.87/72.8	16.4/1373	17.0
	8–7	75.0	77.0	1.27/86.3	26.7/1813	16.5
SO	7_7–6_6	71.0	16.5	0.06/5.0	1.09/91.2	17.7
	8_8–7_7	87.5	18.9	0.27/18.3	4.72/321	21.0
SO_2	$3_{3\,1}$–$2_{2\,0}$	27.6	6.64	0.09/7.5	2.16/181	17.8
	$17_{1\,17}$–$16_{0\,16}$	136	36.5	0.38/31.8	11.3/945	17.9
	$4_{3\,1}$–$3_{2\,2}$	31.3	6.92	0.07/5.3	1.41/107	19.4
	$13_{2\,12}$–$12_{1\,11}$	93.0	13.4	0.25/17.0	6.34/43	16.5
	$5_{3\,3}$–$4_{2\,2}$	35.9	7.32	0.06/4.08	1.36/92.4	16.1
	$14_{4\,10}$–$14_{3\,11}$	136	19.6	0.05/3.40	0.55/37.4	12.1
CS	6–5	49.4	23.1	0.16/14.7	4.12/380	19.1
	7–6	65.8	27.0	0.15/10.2	3.07/209	16.6
^{29}SiO	7–6	57.6	67.2	0.22/18.4	5.08/425	18.7
	8–7	74.1	76.8	0.27/18.3	4.72/321	15.1
^{30}SiO	7–6	56.9	67.2	0.13/12.0	2.06/190	14.1
	8–7	73.2	76.8	0.15/10.2	2.88/196	16.4
HCN	4–3	42.5	108	0.69/15.8	15.3/249	17.0
CN	N = 3–2, J = 5/2–3/2	32.6	6.72	0.08/5.44	1.98/135	18.5
	N = 3–2, J = 7/2–5/2	32.7	9.01	0.07/4.76	1.60/109	18.7

Notes. The third column gives the upper energy level and the fourth column the line strength. The fifth and sixth column yield the peak values and integrated intensity values derived from the observed line profiles. In the last column, the expansion velocity is derived from the expanding shell fit. For the peak flux and the integrated intensity, the values derived from the main-beam temperature (T_{MB}) and the mean brightness temperature estimate (Mean T_b) are given.

The kinetic temperature is assumed to vary as

$$T = T_0 \left[\frac{10^{16}}{r(\mathrm{cm})} \right]^{\alpha} + T_{bg} \,, \tag{5}$$

where T_0 is the temperature at 1×10^{16} cm and T_{bg} represents the background temperature. With the radial profiles for density and temperature given by Eqs. (4) and (5), the program solves for the molecular excitation as a function of radius. Besides collisional excitation, radiation from the cosmic microwave background and thermal radiation from local dust were taken into account. Then, the molecular emission is integrated in radial direction over the line of sight and convolved with the appropriate antenna beam.

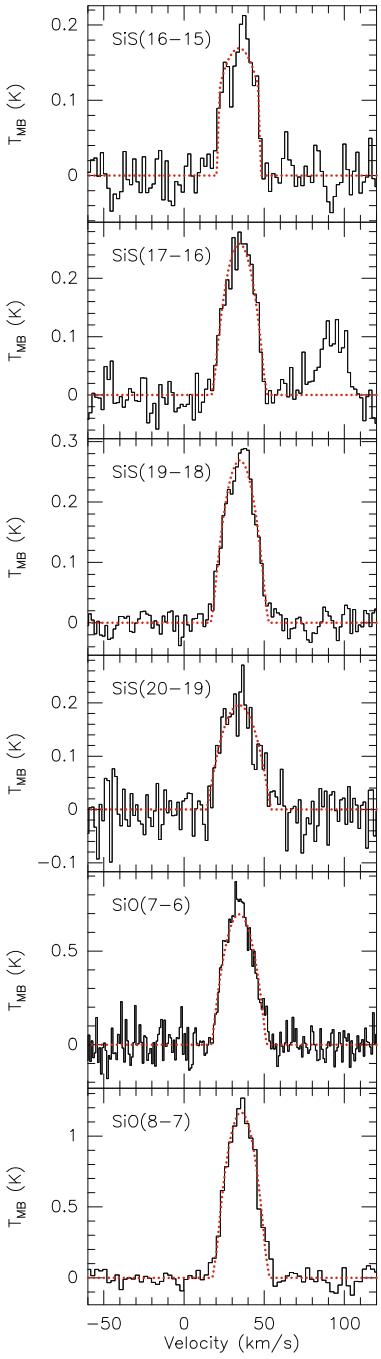

Fig. 4. Observed SiS and SiO line profiles (solid lines) and the expanding shell fit (dotted lines).

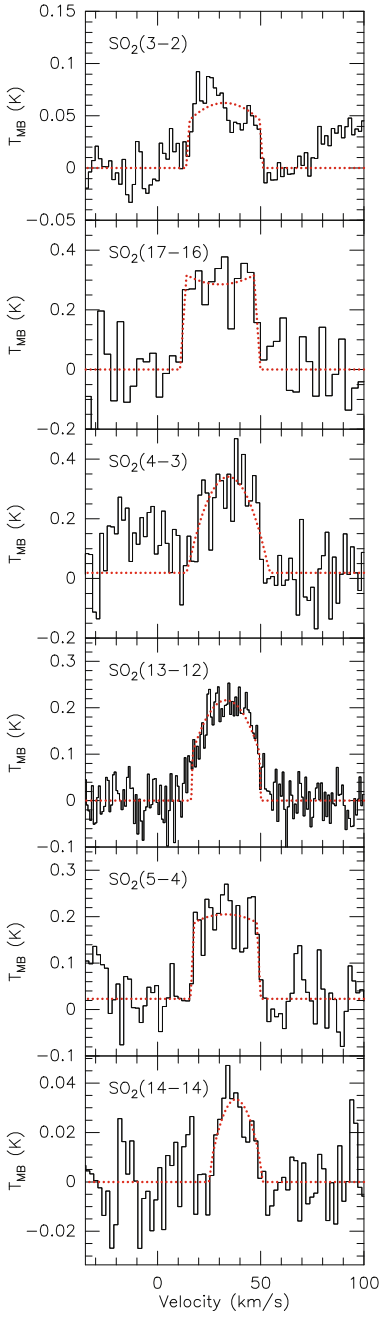

Fig. 5. Observed SO_2 line profiles (solid lines) and the expanding shell fit (dotted lines).

The best-fit model is found by minimizing the total χ^2 using the χ^2 statistic defined as

$$\chi^2 = \sum_{i=1}^{N} \frac{[I_{\rm mod} - I_{\rm obs}]^2}{\sigma^2}, \quad (6)$$

where $I_{\rm mod}$ is the line intensity of the model, $I_{\rm obs}$ the observation, σ the *rms* noise of the observed spectra. The summation is done over all channels N of the three ^{12}CO line transitions as observed for this project with APEX, i.e., $J = 3{-}2$, $J = 4{-}3$, and $J = 7{-}6$. We put more weight on the reproduction of the line shapes and the fitting of the lines observed with the APEX telescope, and they were calibrated in a more consistent way than on the reproduction of the lines taken from the literature. The reduced χ^2 for the models is given by

$$\chi^2_{\rm red} = \frac{\chi^2}{\rm d.f.}, \quad (7)$$

where d.f. is the degree of freedom being $N - p$, with p the number of adjustable parameters. Figure 10 shows the χ^2 contour plot produced by varying the mass-loss rate and the temperature T_0. In this figure, the 68% confidence limit is indicated, i.e. the 1σ level. In this region, the temperature T_0 ranges between 34 to 47 K, and the mass-loss rate is in the range 4.0×10^{-6} to 5.7×10^{-6} $M_\odot$/yr.

The best-fit model parameters are listed in Table 5. The results of the model fits are shown in Fig. 11. In Fig. 12 theoretical

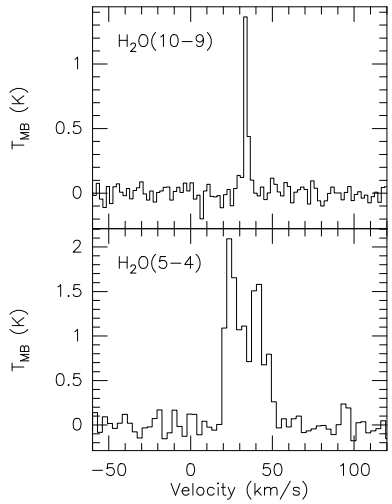

Fig. 6. 321 GHz and 325 GHz H_2O maser emissions observed towards IK Tau.

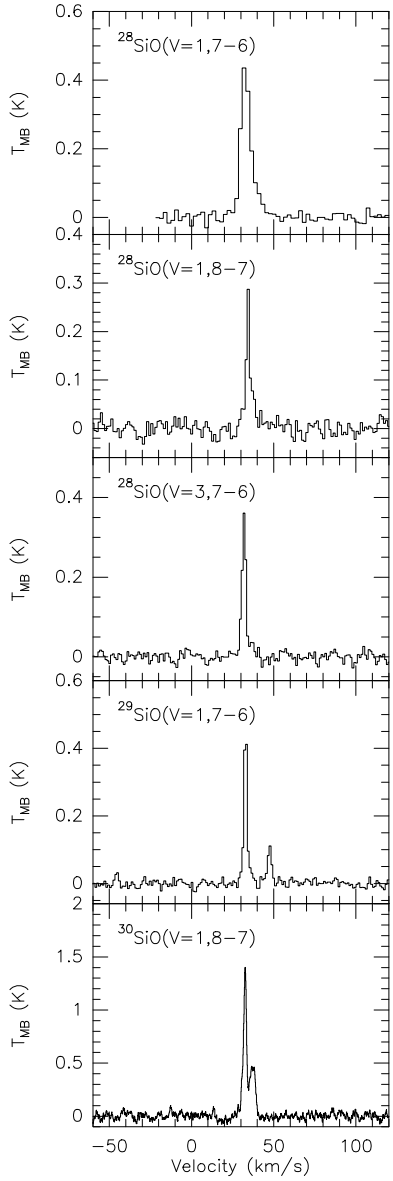

Fig. 7. ^{28}SiO, ^{29}SiO and ^{30}SiO maser emission detected in the rotational transitions J = 7–6 and J = 8–7 of the fundamental v = 1 and v = 3 vibrational excited states observed towards IK Tau.

model predictions for the ^{12}CO lines are shown with different inner radii, different T_0, and different outer radii. Predictions for ^{13}CO with different T_0 are presented in Fig. 13. Predictions for intensities at the observed offset positions were done from the best-fit model and are consistent with the size determined from the observed CO maps.

As shown in Fig. 11, the overall line profiles are fit very well for the higher J transitions (^{12}CO(3−2), ^{12}CO(4−3), ^{12}CO(7−6)). However, the model intensities of the IRAM ^{12}CO(1−0) and ^{12}CO(2−1) transitions are somewhat higher than the observational data taken from the literature, but the shapes fit satisfactorily. The predictions for the ^{12}CO(2−1) line are still within the absolute uncertainty of the line, but this is not the case for the ^{12}CO(1−0) line. An obvious reason for this mismatch could be a problem with the outer radius value. However, our sensitivity analysis (see Fig. 12 and see discussion in next paragraphs) shows that, while lowering the outer radius value indeed the total integrated intensity decreases, the line shape is not reproduced well anymore. Since the relative uncertainty (i.e., the line shape) is much lower than the absolute intensity (i.e., the integrated intensity), we put more weight on the reproduction of the line shapes. Moreover, we note that this is not the first time that an incompatability of the IRAM fluxes with other observed data is reported (e.g. Decin et al. 2008). The ^{13}CO(3−2) line clearly shows a double-horn profile and the best-fit results in a somewhat different T_0 and a different outer radius than for the ^{12}CO data. Nevertheless, the best-fit value for T_0 derived from ^{12}CO still gives a reasonable fit to the ^{13}CO line (Fig. 13). As shown in Fig. 13, the intensities of the profiles do not change so much with T_0, but the lines show a flat shape on top for the lower temperatures (30 K and 40 K), and a double-horn shape at higher temperatures.

As shown in Fig. 12, the line shapes and intensities for all transitions are not influenced much by the inner radius variations since the ^{12}CO emission dominanting the spectra arises from regions farther out in the envelope. The outer radius variations mainly affect the ^{12}CO(1−0) line, which is formed farther out in the envelope than the other ^{12}CO transitions.

4.2. Chemical abundance structure

As explained in the introduction, the density distribution of each molecule is different, depending on the chemical processes taking place: in the envelope. The *fractional abundance* of a species A is usually specified as

$$f_{\rm A}(r) = \frac{n_{\rm A}(r)}{n_{\rm H_2}(r)}, \tag{8}$$

where $n_{\rm H_2}(r)$ is the number density of H_2 and $n_{\rm A}(r)$ is the number density of species A.

A first-order assessment of the molecular abundance fractions can be obtained by assuming that the envelope structure is in local thermodynamic equilibrium. Assuming a spherically symmetric envelope, the fractional abundance for an optically thin rotational line ($J \rightarrow J-1$) of a linear rotor is given by Olofsson et al. (1991):

$$f_x = 3.8\times10^{-16} T_{\rm MB} \frac{V_{\rm exp}^2 BD}{\dot{M}} \frac{T_{\rm ex}}{\mu_0^2 B_0^2 J^2} \times \exp\left(\frac{h(B_0\times10^9)J(J+1)}{kT_{\rm ex}}\right) \frac{1}{\int_{x_{\rm i}}^{x_{\rm e}} \exp(-4\ln 2x^2){\rm d}x} \tag{9}$$

Table 5. Parameters for the best-fit model to the observed ^{12}CO and ^{13}CO line profiles.

	R_i (10^{14} cm)	R_{out} (10^{14} cm)	Mass-loss late ($M_\odot$ yr^{-1})	f_{CO} (10^{-4})	V_{exp} (km s^{-1})	T_0 (K)	α	T_{bg} (K)
^{12}CO	1	630	4.7×10^{-6}	3	18	40	0.8	2.7
^{13}CO	1	700	4.7×10^{-6}	0.35	18	50	0.8	2.7

Notes. R_i represents the inner radius of the envelope, R_{out} the outer radius and f_{CO} = [CO/H$_2$] the CO abundance relative to H$_2$. The last three columns give the values for the parameters in Eq. (5). The expansion velocity is derived from the ^{12}CO(3–2) observations.

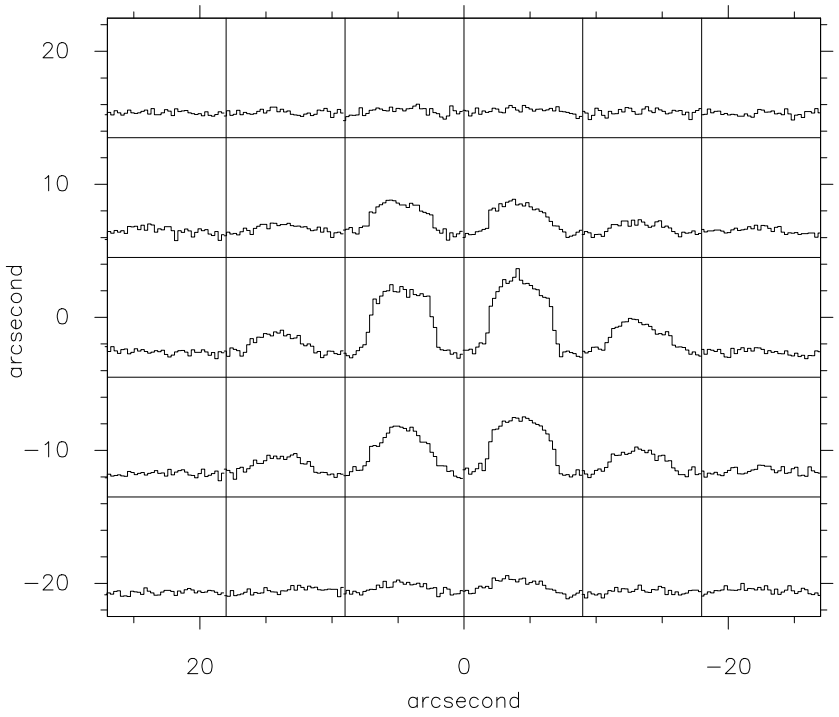

Fig. 8. Map of ^{12}CO J = 3–2 line emission toward IK Tau. The grid spacing was 9″. The main-beam brightness temperatures in the spectra range from 0.5 K to 3.3 K.

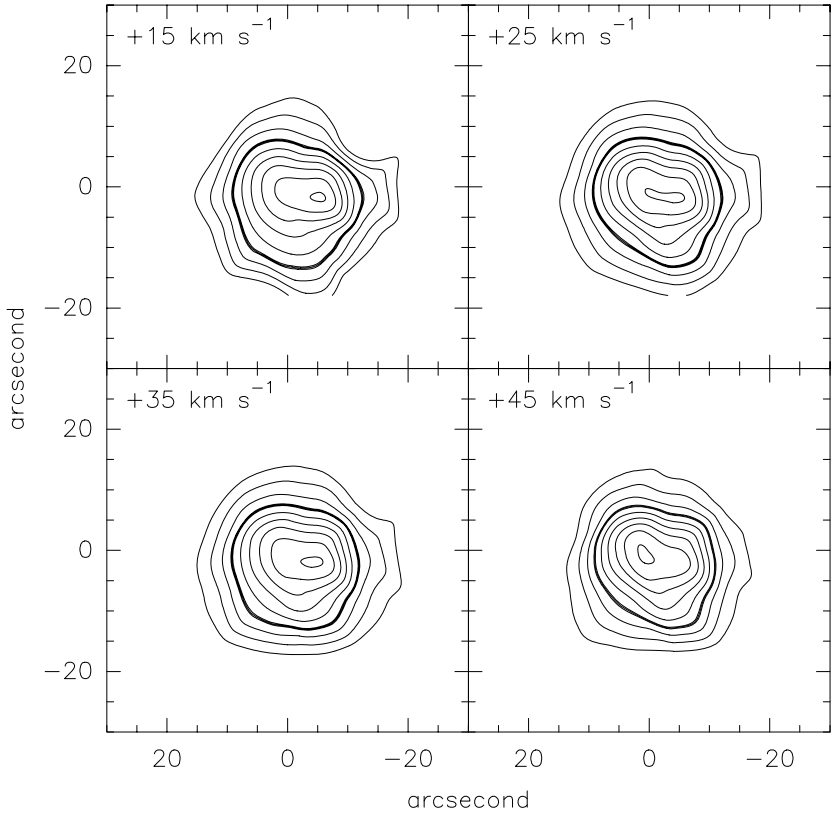

Fig. 9. Contour maps of the ^{12}CO J = 3–2 line emission for IK Tau integrated over 10 km s^{-1} centered at velocities of 15 km s^{-1}, 25 km s^{-1}, 35 km s^{-1}, and 45 km s^{-1}. One velocity interval is centered near the stellar radial velocity of 33.7 km s^{-1}.The contour values are 20% to 90% and 99% of the maximum integrated intensity in each velocity interval, which is 7, 29, 32, and 26 K km s^{-1} for the 15, 25, 35, and 45 km s^{-1} channels, respectively. The 50% contour level is drawn in boldface.

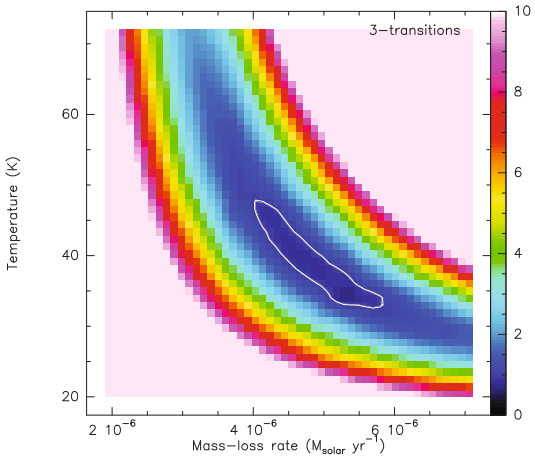

Fig. 10. Reduced χ^2 contour maps of the model to input variable parameters, i.e., the mass-loss rate ($\dot{M}$) and temperature (T_0), which is the kinetic temperature at a given radius (1×10^{16} cm). The contour level is drawn at 0.94 indicating the 68% confidence level.

where $T_{\rm MB}$ is the main-beam brightness temperature, $T_{\rm ex}$ is the excitation temperature (=$T_{\rm rot}$ and equal to the kinetic temperature under the LTE assumption), μ_0 is the dipole moment in Debye, B_0 the rotational constant in GHz, $V_{\rm exp}$ the gas expansion velocity of the CSE in km s^{-1}, B the beam size in arcseconds, D the distance to the source in pc, $\dot{M}$ the mass-loss rate in $M_\odot$ yr^{-1}, and $x_{\rm i}$ (=0) and $x_{\rm e}$ are the inner and outer radii of the CSE, respectively, measured in units of B. It has for simplicity been assumed that f_x is constant from $x_{\rm i}$ to $x_{\rm e}$ and zero elsewhere. For CN, the relative strengths of the different hyperfine components were taken into account. If the line is optically thick, the value of f_x estimated by the above formula is only a lower limit.

The SO_2 abundance with respect to H_2 is estimated using the equation given by Morris et al. (1987):

$$f_{\rm SO_2} = \frac{T_{\rm a}({\rm SO_2})}{2\times10^{13}} \frac{V_{\rm exp}^2 B D Q(T_{\rm ex})}{\dot{M}\mu_0^2 S \nu} \times \frac{1}{\exp[-1.44E_{\rm u}/T_{\rm ex}]} \frac{1}{\int_{x_{\rm i}}^{x_{\rm e}} \exp(-4\ln 2x^2){\rm d}x} \quad (10)$$

where $Q(T_{\rm ex})$ is the molecular partition function ($\simeq 1.15 T_{\rm ex}^{3/2}$, for more detail see Omont et al. 1993), $E_{\rm u}$ is the energy of the upper state of the transition, S the line strength, and ν the frequency of the transition.

A mass-loss rate of $\dot{M} = 4.7 \times 10^{-6}\ M_\odot$ yr^{-1} (see Sect. 4.1, and Teyssier et al. 2006) was adopted to calculate the abundances. Since the outer radius of the molecular emitting region can be quite uncertain for molecules for which no observational maps exist, two different outer radii will be used for these molecules ("case A" and "case B"). For SiO, the value for the outer radius was taken to be 2×10^{15} cm (case A) and 5×10^{15} cm (case B), and for the other molecules 1×10^{16} cm (case A) and 5×10^{16} cm (case B) was assumed (Bujarrabal et al. 1994). For all lines from this work, we adopted expansion velocities from Table 4. For lines taken from the literature (see Table 7), an expanding velocity of 18 km s^{-1} is used that is consistent with our non-LTE CO modeling of the envelope. For the excitation temperatures, $T_{\rm ex}$, rotational temperatures as computed from Boltzmann diagrams are taken (see Table 6). Values for the upper energy level and line strength ($\mu_0^2 S$) can be found in Table 4.

Table 6. Rotational temperature and beam-averaged column density.

Species	$T_{\rm rot}$ (K)	N (cm^{-2})
SiS	85.8 (11.1)	4.46×10^{15} (1×10^{15})
SiO	17.1 (1.0)	8.24×10^{15} (1×10^{15})
SO	27.2 (2.7)	6.35×10^{15} (2×10^{15})
SO_2	67.5 (6.8)	2.02×10^{16} (4×10^{15})
^{30}SiO	68.6 (82.3)	2.48×10^{14} (4×10^{14})
^{29}SiO	30.0 (15.5)	7.12×10^{14} (9×10^{14})
CS	33.9 (4.7)	8.89×10^{14} (2×10^{14})
HCN	8.3 (0.5)	2.27×10^{15} (5×10^{14})

Notes. The temperature and the density were determined from the rotational diagram analysis. The uncertainties are given within parenthesis (no systematic errors included).

4.2.1. Results

Using the method outlined above, the fractional abundances of all molecules (except CO) were determined (see Table 7). The most uncertain parameters used to derive the fractional abundances are $T_{\rm ex}$, D, and $x_{\rm e}$ (the outer radius). Here, $T_{\rm ex}$ is obtained from the rotational diagram analysis, D is taken from the literature, and the outer radius of $x_{\rm e}$ has been adopted differently for each individual molecule. We also note that our analysis assumes optically thin emission, which is not always the case for the studied line profiles. The line opacity is expected to be greater for higher J rotational transitions, so that lower J rotational transitions are expected to better probe the fractional abundance.

5. Discussion

Table 8 and Fig. 14 compare the average abundance of each molecule to values found in the literature. Compared to observational results (Bujarrabal et al. 1994; Lindqvist et al. 1988; Omont et al. 1993), our deduced fractional abundances agree within a factor of 3.5 for the smaller outer radius (case A), and for the larger outer radius (case B) within a factor of 10. Compared to the predicted abundances from theoretical chemical models by Willacy & Millar (1997) and Duari et al. (1999), we found that the predictions are comparable to our deduced values (using the smaller outer radius, case A) within a factor of ~3 for CS and SiO. Our deduced value for the SO, SiO, CN, and SiS fractional abundances agree with the results of Willacy & Millar (1997), but the predicted values by Duari et al. (1999) are much lower. The SO_2 abundance from this work is almost two orders of magnitude higher than the value predicted by Willacy & Millar (1997).

As noted above, the SiS abundance in the chemical models of Duari et al. (1999) is much lower than the observed value. The chemical models by Duari et al. (1999) focus on the inner envelope (within few stellar radii), while Willacy & Millar (1997) studied the chemical processes partaking in the outer envelope. The agreement between our deduced value for the fractional abundance of SiS and the predictions by Willacy & Millar (1997) suggests that SiS is formed in the outer envelope.

The deduced SO abundance is a factor ~10 higher than the inner wind predictions by Duari et al. (1999), but they agree with

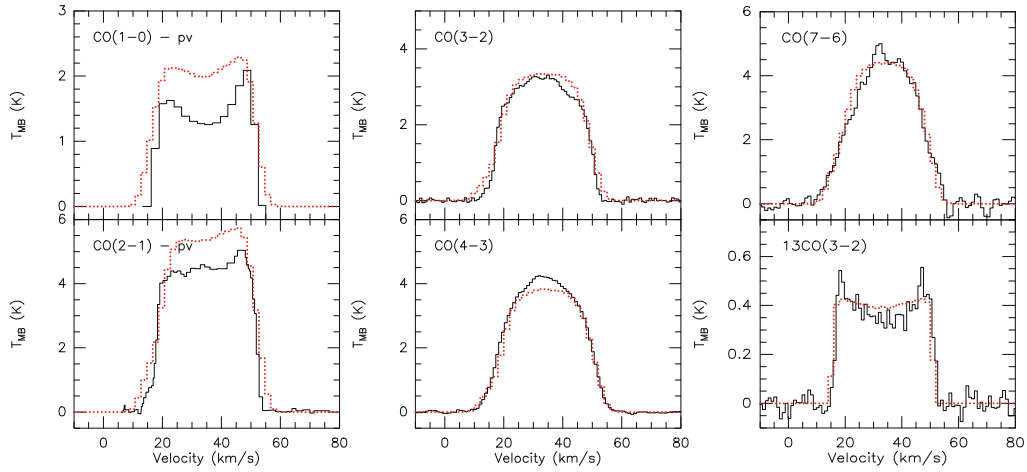

Fig. 11. Best-fit model spectra for the different CO transitions to the available set of data at offset (0″, 0″) for IK Tau. Parameters used to calculate the best-fit theoretical predictions are given in Table 5. The ^{12}CO(1−0) and ^{12}CO(2−1) data are from Teyssier et al. (2006), where "pv" means the IRAM 30 m telescope in Pico Veleta. The model fits are shown by dotted lines.

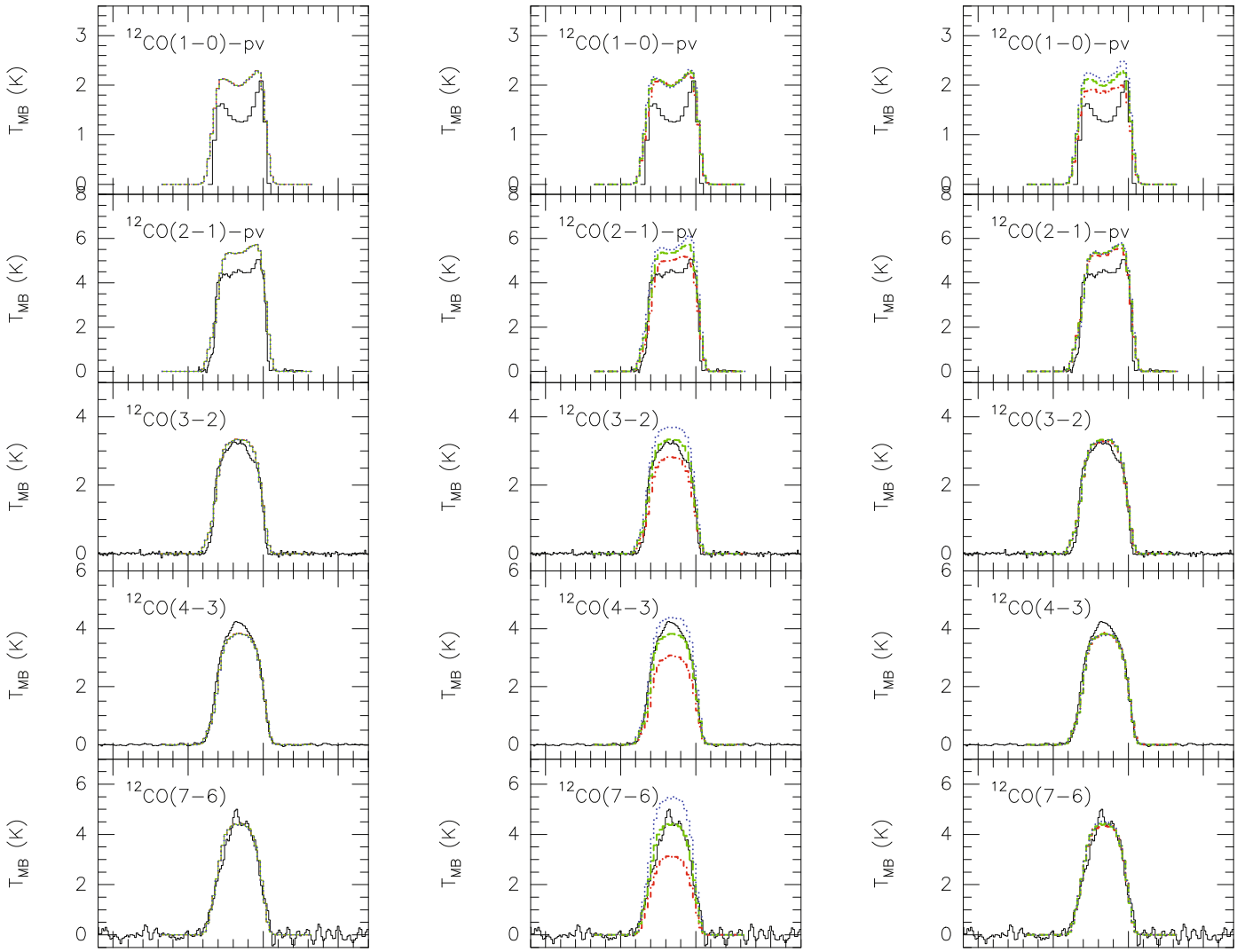

Fig. 12. Model fits with different input parameters to the set of data at offset (0″, 0″) for IK Tau. *Left column* shows variations in the inner radius: 0.1×10^{14} cm (dash-dotted line), 1×10^{14} cm (dashed line), 10×10^{14} cm (dotted line). *Middle column* shows variation in T_0: 30 K (dash-dotted line), 40 K (dashed line), 50 K (dotted line). *Right column* shows variations in the outer radius: 5.3×10^{16} cm (dash-dotted line), 6.3×10^{16} cm (dashed line), 7.3×10^{16} cm (dotted line).

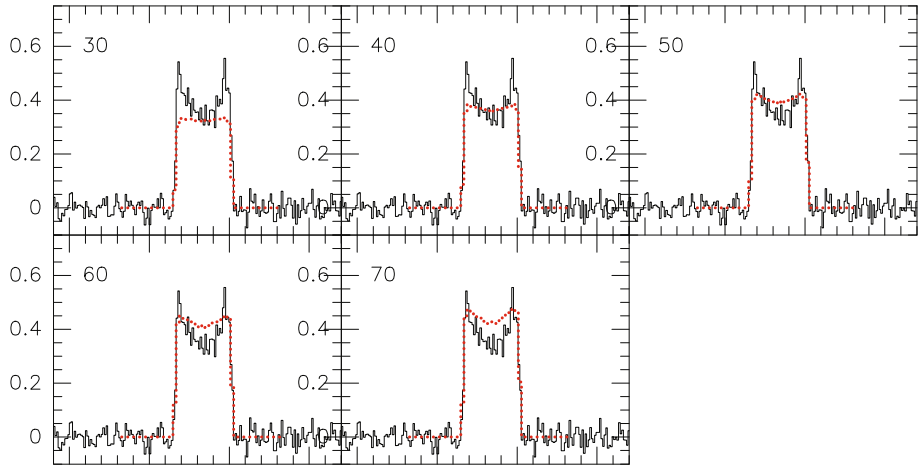

Fig. 13. Model fits of the ^{13}CO(3–2) transition with different values for T_0, as indicated in the *upper left corner* of each panel. The model fits are shown by dotted lines.

Table 7. Derived molecular fractional abundance for each transition.

Species	Transition	Abundance (case A)	Outer radius (case A)	Abundance (case B)	Outer radius (case B)	Reference
SiS	(5–4)	1.5×10^{-6}	1×10^{16}cm	3.8×10^{-7}	5×10^{16}cm	(1)
	(16–15)	6.0×10^{-7}		1.7×10^{-7}		
	(17–16)	1.2×10^{-6}		3.6×10^{-7}		
	(19–18)	1.3×10^{-6}		4.2×10^{-7}		
	(20–19)	1.7×10^{-6}		5.4×10^{-7}		
SiO	(2–1)	1.7×10^{-5}	2×10^{15}cm	6.7×10^{-6}	5×10^{15}cm	(1)
	(3–2)	1.5×10^{-5}		6.2×10^{-6}		(1)
	(5–4)	3.8×10^{-6}		1.5×10^{-6}		(2)
	(7–6)	8.3×10^{-6}		3.3×10^{-6}		
	(8–7)	1.9×10^{-5}		7.6×10^{-6}		
SO	(2_2–1_1)	2.0×10^{-7}	1×10^{16}cm	5.2×10^{-8}	5×10^{16}cm	(2)
	(5_6–4_5)	1.1×10^{-6}		4.3×10^{-7}		(1)
	(7_7–6_6)	2.3×10^{-7}		6.6×10^{-8}		
	(8_8–7_7)	1.6×10^{-6}		5.1×10^{-7}		
SO_2	($3_{1\,3}$–$2_{0\,2}$)	1.7×10^{-5}	1×10^{16}cm	4.3×10^{-6}	5×10^{16}cm	(2)
	($10_{1\,9}$–$10_{0\,10}$)	1.1×10^{-5}		2.9×10^{-6}		(2)
	($10_{0\,10}$–$9_{1\,9}$)	1.6×10^{-5}		5.1×10^{-6}		(2)
	($3_{3\,1}$–$2_{2\,0}$)	6.0×10^{-6}		1.7×10^{-6}		
	($17_{1\,17}$–$16_{0\,16}$)	4.7×10^{-5}		1.4×10^{-5}		
	($4_{3\,1}$–$3_{2\,2}$)	4.8×10^{-6}		1.5×10^{-6}		
	($13_{2\,12}$–$12_{1\,11}$)	2.1×10^{-5}		6.5×10^{-6}		
	($5_{3\,3}$–$4_{2\,2}$)	2.5×10^{-6}		8.0×10^{-7}		
	($14_{4\,10}$–$14_{3\,11}$)	3.8×10^{-6}		1.2×10^{-6}		
^{30}SiO	(7–6)	2.2×10^{-6}	2×10^{15}cm	8.7×10^{-7}	5×10^{15}cm	
	(8–7)	6.7×10^{-6}		2.8×10^{-6}		
^{29}SiO	(7–6)	6.2×10^{-6}	2×10^{15}cm	2.5×10^{-6}	5×10^{15}cm	
	(8–7)	1.1×10^{-5}		4.6×10^{-6}		
CS	(2–1)	4.7×10^{-7}	1×10^{16}cm	1.1×10^{-7}	5×10^{16}cm	(3)
	(3–2)	1.9×10^{-7}		5.9×10^{-8}		(1)
	(6–5)	3.2×10^{-7}		9.2×10^{-8}		
	(7–6)	2.0×10^{-7}		6.3×10^{-8}		
HCN	(1–0)	4.9×10^{-7}	1×10^{16}cm	1.3×10^{-7}	5×10^{16}cm	(1)
	(4–3)	2.3×10^{-6}		7.2×10^{-7}		
CN	N = 3–2, J = 5/2–3/2	9.8×10^{-8}	1×10^{16}cm	3.1×10^{-8}	5×10^{16}cm	
	N = 3–2, J = 7/2–5/2	2.3×10^{-7}		7.1×10^{-8}		

Notes. For some molecules, other line transition were searched in the literature.
References. (1) Bujarrabal et al. (1994); (2) Omont et al. (1993); (3) Lindqvist et al. (1988).

Table 8. Comparison of the derived molecular fractional abundances with other published results.

	CS	HCN	SiO	SiS	SO	SO_2	CN
This work (case A)	3.0×10^{-7}	1.4×10^{-6}	1.3×10^{-5}	1.3×10^{-6}	7.8×10^{-7}	1.4×10^{-5}	1.6×10^{-7}
This work (case B)	8.1×10^{-8}	4.3×10^{-7}	5.1×10^{-6}	3.7×10^{-7}	2.7×10^{-7}	4.2×10^{-6}	5.1×10^{-8}
(1)	1.0×10^{-7}	9.8×10^{-7}	1.7×10^{-5}	4.4×10^{-7}	2.6×10^{-6}	–	–
(2)	3.0×10^{-7}	6.0×10^{-7}	–	7.0×10^{-7}	–	–	–
(3)	–	–	3.0×10^{-6}	–	1.8×10^{-6}	4.1×10^{-6}	–
(4)	2.9×10^{-7}	1.4×10^{-7}	3.2×10^{-5}	3.5×10^{-6}	9.1×10^{-7}	2.2×10^{-7}	3×10^{-7}
(5)	2.8×10^{-7}	2.1×10^{-6}	3.8×10^{-5}	3.8×10^{-10}	7.8×10^{-8}	–	2.4×10^{-10}

Notes. In the first part, we list results derived from an observational analysis, in the second part theoretical predictions from chemical models. Abundances from the chemical models by Duari et al. (1999) were selected at a radius of $2.2R_*$ (5×10^{13} cm).

References. (1) Bujarrabal et al. (1994); (2) Lindqvist et al. (1988); (3) Omont et al. (1993); (4) Willacy & Millar (1997); (5) Duari et al. (1999).

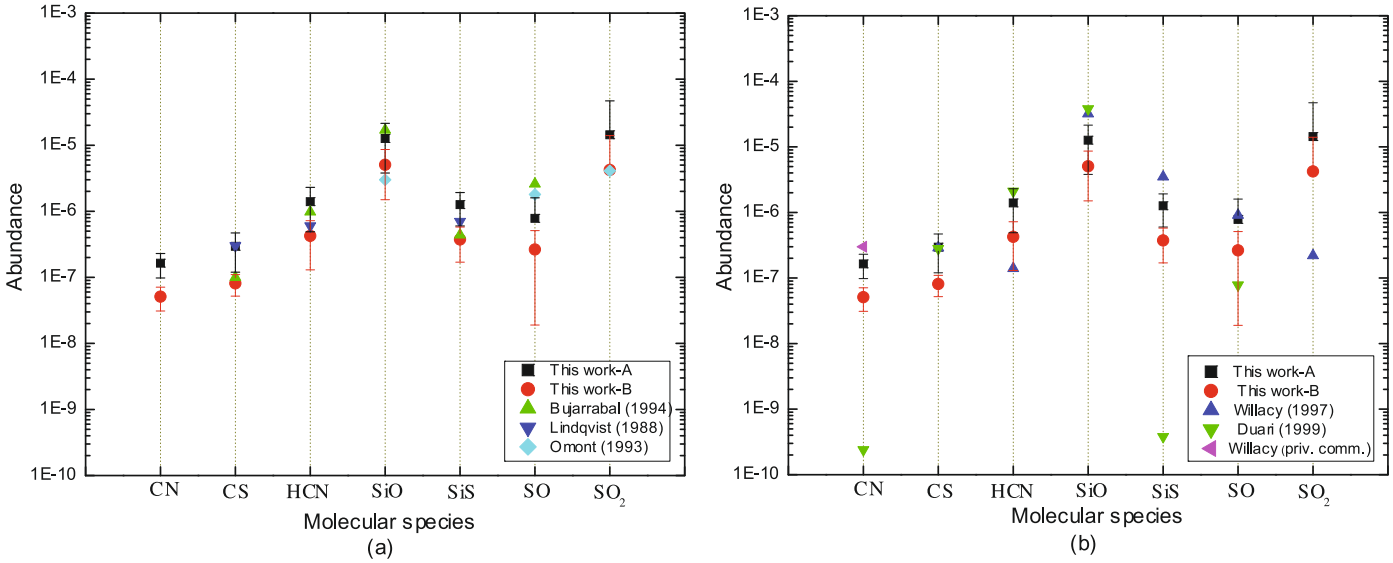

Fig. 14. Comparison of the molecular fractional abundances derived in this work (case A and case B-study) and values found in the literature (Bujarrabal et al. 1994; Lindqvist et al. 1988; Omont et al. 1993; Willacy & Millar 1997; Duari et al. 1999). The errors are estimated from the abundance variations for the different transitions (see Table 8). Panel **a)** gives a comparison to other observational results, panel **b)** to chemical model predictions.

the outer wind predictions by Willacy & Millar (1997). Willacy & Millar (1997) assumed no SO injection, but only in-situ formation. CN is clearly produced in the outer envelope, as a photodissociation product of HCN.

The abundance of SO_2 found by Willacy & Millar (1997) is much lower than the observed ones. A value of 1.4×10^{-5} (case A) means that SO_2 contains 80% of the solar sulfur value. Willacy & Millar (1997) suggest that SO_2 may be formed in a different part of the envelope compared to the other sulfur-bearing molecules, for example, in shocks in bipolar outflow or in the inner envelope. An indication for the typical behavior of SO_2 also comes from the line profiles; e.g., the SO_2 (14–14) line is clearly narrower and shifted to the red.

The SiO abundance derived in this study is close to the abundance predicted by the theoretical chemical models. Cherchneff (2006) investigated the nonequilibrium chemistry of the inner winds of AGB stars and derived an almost constant, high SiO abundance (about 4×10^{-5} before the condensation of dust). Duari et al. (1999) and Willacy & Millar (1997) derived 3.8×10^{-5} and 3.2×10^{-5} for the inner and outer winds, respectively. Furthermore, González Delgado et al. (2003) performed an extensive radiative transfer analysis of circumstellar SiO emission from a large sample of M-type AGB stars, where they adopted the assumption that the gas-phase SiO abundance stays high close to the star, and farther out the SiO molecular abundance fraction decreases due to absorption onto dust grains. Their results show that the derived abundances are always below the abundances expected from stellar atmosphere equilibrium chemistry. For a mass-loss rate of 4×10^{-6} $M_\odot$/yr, the equilibrium chemistry abundance of SiO is $\sim 3.5 \times 10^{-5}$ (Cherchneff 2006). Taking the scenario of depletion due to dust formation into account, the higher excitation SiO(8–7) would probe a higher SiO abundance. As seen in Table 7, the SiO(8–7) indeed probes a higher fractional abundance, although not significantly higher than the other lines.

6. Conclusions

In this work, we present for the (sub)millimeter survey for an oxygen-rich evolved AGB star, IK Tau, in order to study the chemical composition in the envelope around the central target. An extensive non-LTE radiative transfer analysis of

circumstellar CO was performed using a model with a power-law structure in temperature and density and a constant expansion. The observed line profiles of ^{12}CO(3−2), ^{13}CO(3−2), ^{12}CO(4−3), and ^{12}CO(7−6) are fit very well by our model, yielding a mass-loss rate of 4.7×10^{-6} $M_{\odot}$/yr. The line shapes and intensities for all ^{12}CO transitions are not influenced much by variations in the inner radius, which is understandable since the bulk of the ^{12}CO emission is produced in the outer envelope. The intensities for the higher excitation CO lines depend strongly on the assumed temperature but not on the value of the outer radius.

For 7 other molecules (SiO, SiS, HCN, CS, CN, SO, and SO_2) a fractional abundance study based on the assumption of LTE is performed. A full non-LTE analysis of all molecules is beyond the scope of this observational paper, but will be presented in a next paper (Decin et al. 2010). This study shows that IK Tau is a good laboratory to study the conditions in circumstellar envelopes around oxygen-rich stars with submillimeter-wavelength molecular lines. The improved abundance estimates of this study will allow refinements of the chemical models in the future.

Molecular line modeling predicts the abundance of each molecule as a function of radial distance from the star, although some ambiguity about an inner or outer wind formation process often exists. To get a clear picture of the different chemistry processes partaking in the different parts in the envelope, mapping observations for molecules other than CO should be performed. Since most of the submillimeter emission from molecules less abundant than CO probably arises from the inner part of the envelope at 2–4″, meaningful observations require interferometers such as the future Atacama Large Millimeter Array (ALMA).

Acknowledgements. This publication is based on data acquired with the Atacama Pathfinder Experiment (APEX). APEX is a collaboration between the Max-Planck-Institut für Radioastronomie, the ESO, and the Onsala Space Observatory. We are grateful to the APEX staff for their assistance with the observations. L.D. acknowledges support from the Fund of Scientific Research, Flanders, Belgium.

References

Alcolea, J., Pardo, J., & Bujarrabal, V. 1999, ApJ, 139, 461
Bachiller, R., Fuente, A., Bujarrabal, V., et al. 1997, A&A, 319, 235
Bernes, C. 1979, A&A, 73, 67
Boboltz, D., & Diamond, P. 2005, A&A, 625, 978
Bowers, P. F., Johnston, K. J., & Spencer, J. H. 1983, ApJ, 274, 733
Bowers, P. E., Johnston, K. J., & de Vegt, C. 1989, ApJ, 340, 479
Bujarrabal, V., & Alcolea, J. 1991, ApJ, 251, 536
Bujarrabal, V., Fuente, A., & Omont, A. 1994, ApJ, 285, 247
Cernicharo, J., Guélin, M., & Kahane, C. 2000, A&AS, 142, 181
Cherchneff, I. 2006, A&A, 456, 1001
Decin, L., Blomme, L., Reyniers, M., et al. 2008, A&A, 484, 401
Decin, L., De Beck, E., Brünken, S., et al. 2010, A&A, 516, A69
Duari, D., Cherchneff, I., & Willacy, K. 1999, ApJ, 341, L47
Fukasaku, S., Hirahara, Y., Masuda, A., et al. 1994, ApJ, 437, 410
Gautschy-Loidl, R., Höfner, S., Jørgensen, U., & Hron, J. 2004, A&A, 422, 289
Goldreich, P., & Scoville, N. 1976, ApJ, 205, 144
González Delgado, D., Olofsson, H., Kerschbaum, F., et al. 2003, A&A, 411, 123
Güsten, R., Nyman, L., Schilke, P., et al. 2006, A&A, 454, L13
Habing, H. 1996, A&ARv, 7, 97
Hale, D. D. S., Bester, M., Danchi, W. C., et al. 1997, ApJ, 490, 407
Heyminck, S., Kasemann, C., Güsten, R., et al. 2006, A&A, 454, L21
Hogerheijde, M., & van der Tak, F. 2000, ApJ, 362, 697
Lane, A., Johnston, K., Bowers, P., et al. 1987, ApJ, 323, 756
Lindqvist, M., Nyman, L.-A., Olofsson, H., & Winnberg, A. 1988, ApJ, 205, L15
Lucas, R., Bujarrabal, V., Guilloteau, S., et al. 1992, ApJ, 262, 491
Mamon, G. A., Glassgold, A. E., & Huggins, P. J. 1988, ApJ, 328, 797
Marvel, K. 2005, AJ, 130, 261
Morris, M., Guilloteau, S., Lucas, R., & Omont, A. 1987, ApJ, 321, 888
Olofsson, H., Lindqvist, M., Nyman, L.-A., et al. 1991, ApJ, 245, 611
Olofsson, H., Lindqvist, M., Nyman, L., & Winnberg, A. 1998, A&A, 329, 1059
Omont, A., Lucas, R., Morris, M., & Guilloteau, S. 1993, ApJ, 267, 490
Ridgway, S. T., Hall, D. N. B., Wojslaw, R. S., Kleinmann, S. G., & Weinberger, D. A. 1976, Nature, 264, 345
Risacher, C., Vassilev, V., Monje, R., et al. 2006, A&A, 454, L17R
Smith, N., Humphreys, R., Davidson, K., et al. 2001, AJ, 121, 1111
Sopka, R. J., Hildebrand, R., Jaffe, D. T., et al. 1985, ApJ, 294, 242
Teyssier, D., Hernandez, R., Bujarrabal, V., et al. 2006, A&A, 450, 167
Willacy, K., & Millar, T. 1997, A&A, 324, 237
Wing, R., & Lockwood, G. 1973, ApJ, 184, 873
Yamamura, I., Onaka, T., Kamijo, F., et al. 1996, ApJ., 465, 926
Ziurys, L., Milam, S., Apponi, A., & Woolf, N. 2004, Nature, 447, 1094
Zuckerman, B. 1987, IAUS, 120, 345